# A stereoscopic method for rapid monitoring of the spatio-temporal evolution of the sand-bed elevation in the swash zone

D. Astruc [a,b,1], S. Cazin [a,b,1], E. Cid [a,b,1], O. Eiff [a,b,1], L. Lacaze [a,b,1,*], P. Robin [a,b,1], F. Toublanc [a,b,1], I. Cáceres [c]

[a] Université de Toulouse; INPT, UPS; IMFT(Institut de Mécanique des Fluides de Toulouse); Allée Camille Soula, F-31400 Toulouse, France
[b] CNRS; IMFT; F-31400 Toulouse, France
[c] Laboratori d'Enginyeria Marítima, Universitat Politècnica de Catalunya, Jordi Girona, 1-3, 03034 Barcelona, Spain

A B S T R A C T

A stereoscopic technique is developed in order to measure the sand-bed elevation in the swash zone at the wave time-scale. The present technique allows one to perform highly resolved measurements both in time and in space. An accuracy and a precision of less than 300 μm and 600 μm, respectively, are obtained in each direction. This technique has been used during a large-scale wave flume experiment where an erosive process of a plane beach is studied. The stereoscopic technique allows one to accurately measure the long-term evolution of the beach profile. In addition, spatially dependent variability on shorten time-scales is observed featuring accretion as well as erosion at the wave time-scale.

*Keywords:*
Swash zone
Stereovision
Morphodynamics
Bed evolution

## 1. Introduction

The swash zone is the transitional zone between the surf zone and the subaerial dry beach. This zone is known to be alternatively covered and uncovered by water which makes it difficult to be instrumented for both hydrodynamical and bed-shape measurements. The nearshore area, including the surf zone and the swash zone, experiences strong hydrodynamic forcing and sediment transport due to a highly complex hydrodynamical system spanning from wave breaking to the uprush and backwash within the swash zone (Longo et al., 2002). These large sand motions are responsible for the bar formation in the surf zone (Lippmann and Holman, 1990) as well as erosion or accretion of coastal beaches, an important issue in coastal management and preservation. It is now admitted that sediment transport rates are much larger in the swash zone than in the surf zone, the swash zone therefore being the most dynamic region of the nearshore (Masselink and Puleo, 2006). Moreover, as the swash zone ends at the shoreline position, knowledge of its dynamics is fundamental to predict the evolution of coastal areas.

Even if several reviews on the subject are now available in the literature (Butt and Russell, 2000; Elfrink and Baldock, 2002; Masselink and Puleo, 2006), the dynamics of the swash zone remains not fully understood due to its complexity. First, the swash zone hydrodynamics is not symmetric as the flow is decelerating during uprush and accelerating during backwash. This asymmetry induces a strong difference in the transport processes between the two regimes. Moreover, even if the transport rates are large in the swash zone, the net transport during a complete wave event is a small quantity. As mentioned by Elfrink and Baldock (2002), this last point also makes quantification of transport difficult in the swash zone. Moreover, infiltration and exfiltration of water through the beach surface can also modify the local structure of the boundary layer at the beach face and have thus the potential to affect the sediment transport in the swash zone, altering for instance the critical Shields parameter defining the transition from rest to bed load transport (Elfrink and Baldock, 2002). Again, filtration measurements are difficult to perform and are thus poorly documented in the literature. The swash zone is thus a complex and strongly coupled system involving several processes. Field and lab measurements are therefore needed to improve the modelling of the nearshore evolution.

Several developments in field measurements can yield important and valuable data of real situations (Aagaard and Hughes, 2010; Baldock et al., 2006; Masselink et al., 2005; Turner et al., 2008), yet it remains difficult to dissociate a great number of phenomena from essential mechanisms under uncontrolled conditions. Also, it remains more difficult to collect highly resolved and robust measurements in the field, since the measurements themselves are influenced by the uncontrolled conditions. A valuable alternative is offered by large-scale laboratory experiments which are more easily controlled and are reproducible, but also in close similitude to nature due to their size. As mentioned above, one of the main difficulties in measuring the swash zone is the coexistence of three phases (sand, water and air). Further, each point of the swash zone can be emerged or submerged. Finally, one of the key points in quantifying erosion or accretion of the beach is the sand-bed position. Therefore, a first step to estimate the sand transport rate is the measurement of the emerged bed position resulting from the

* Corresponding author.
*E-mail addresses:* lacaze@imft.fr, Laurent.Lacaze@imft.fr (L. Lacaze).
[1] This work is a collaborative effort: these authors are listed by alphabetical order.

wave forcing (uprush and backwash processes). Traditional mechanical methods to investigate the bed-shape evolution suffer at least from two limitations. First, they are intrusive, implying that measurements can only be performed when the wave cycle is stopped, and second, they will always deform the bed to some degree whilst being limited to a single profile or a series of profiles due to the amount of time needed to perform the measurements. Although the global bed-shape evolution can be obtained by this method, certainly of interest, the actual sediment transport resulting from a given wave or wave group cannot be obtained, as this needs to resolve the bed evolution during a single wave cycle. Another alternative is the acoustic sensor which allows a time-resolved measurement of the bed position (Turner et al., 2008). However, this technique only gives access to a point measure of the sand-bed position. Optical techniques have also been started to be developed for in-situ measurements of the sand-bed surface elevation in the swash zone (Holland and Puleo, 2001). A stereometric optical method allows these authors to reconstruct the three-dimensional positions of the water front (swash edge) as a function of time. The temporal evolution of the edge position then leads to the cross-shore evaluation of the sand bottom in the swash zone. The estimated accuracy on the surface elevation was around 2 cm in their study (Holland and Holman, 1997).

In the present study, an optical method has been developed to measure the emerged sand-bed surface elevation as part of the Hydralab III/SANDS campaign in the large-scale flume *Canal de Investigación y Experimentación Marítima* (CIEM) at the *Universidad Politécnica de Catluña* in Barcelona. The method is non-intrusive, leading to an accuracy of the height estimation of the order of the sand grain size whilst the temporal resolution allows the wave cycle to be captured. The chosen principle is to reconstruct the bed-surface elevation via stereoscopic imaging from two different view points by correlating matched projected points on the beach. The stereoscopic technique has been used during a wave flume experiment where wave forcing characterised by a Jonswap spectrum eroded an initially 1/15 slope plane beach.

The manuscript is organised as follows. First, the optical sterovision techniques developed are presented in Section 2. Estimations of the errors are also given. A first set of results, which were obtained within the SANDS campaign in 2008, demonstrating the applicability and interest of the technique are then shown and discussed in Section 3. Finally, conclusions are drawn.

## 2. Technical methodology

The technique is based on the determination of the position of a set of points on the beach, in the laboratory frame of reference, via their imaged positions in the image planes of two separate cameras. The three-dimensional position of these points at different times thus yields quantitative information on the bed evolution in the swash zone. Such a technique, known as stereovision, is widely used for recovering 3D structures of a scene and has been used very recently to evaluate the interface elevation of free surface flows (Chatellier et al., 2010; Douxchamps et al., 2005; Jehle et al., 2008) for instance.

If one considers a point $P$ in the laboratory frame of reference (i.e. the world coordinates) imaged by two cameras, here referred to as cameras 1 and 2 (fixed in the laboratory frame of reference and not aligned), the process to determine its position $P_{|w} = (x_w, y_w, z_w)$ in the world coordinate frame of reference is known as triangulation. Triangulation is the identification of the intersecting point between the two different lines of sight –rays– passing through the two image points of $P$, $P^1$ and $P^2$ and with $O^1$ and $O^2$ the centres of the optical systems associated with cameras 1 and 2, respectively, as will be explained in Section 2.3 (see Fig. 1).

This procedure thus gives access to the third spatial dimension, lost by imaging a scene with only one camera, using the information from both cameras.

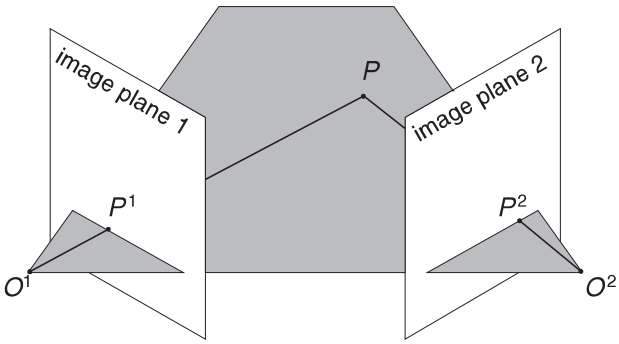


**Fig. 1.** Binocular stereovision configuration. The two image points $P^1$ and $P^2$ of the point $P$ are located on the line of sight of each camera.

### 2.1. Experimental set-up

One of the major issues of a stereovision technique is its implementation on a large scale experimental device such as CIEM. Here, the area of interest is relatively large (a 3 m × 2 m field). A first concern is thus minimising optical distortion and achieving good resolution of the recorded field. To this end, two synchronised high-resolution, high-sensitivity 14-bit PCO-2000 cameras (2048 × 2048 pix$^2$ with a CCD cell size of 7.4 × 7.4 μm$^2$) were chosen, coupled to 24 mm Nikon lenses ($f$ = 24 mm). To eliminate vibrations, the cameras were attached on a rigid and strong aluminium structure, the distance between the cameras and from the zone of interest being about $T$ = 4.5 m and $D$ = 5 m, respectively (see Fig. 2). The two cameras thus recorded the same field with an angle between the two line of sights of around 50°. To optimise the imaged field and limit distortion differences between the two cameras, the line between the two cameras is parallel to the initial 1/15 slope of beach (see Fig. 2).

### 2.2. Detection of specific points on the surface of the swash zone

The first step of the experimental technique is to detect the two image-points of each point $P_k$ ($k$ being the index of each point) of the set on the bed surface of the swash zone recorded by the two cameras. The image-points obtained from the two view sights then have to be matched for each $P_k$. As a sand-bed does not exhibit sufficient texture at large image scale (several meters), a regular grid of light dots (1470 dots) was projected onto the swash zone (a 3 × 2 m$^2$ area) from the top (see Fig. 3), each dot having a radius of about 2 cm. The grid is projected using a 2000 lm video projector mounted between the two cameras (see Fig. 2). The points $P_k$ are then considered to be the centre of each dot, $k$ = 1 : 1470. The horizontal resolution of the measurement is controlled by the distance between each dot which is about 5 cm.

It is worth noting that the swash zone divides into a dry zone (right part of the camera images in Fig. 3) and a wet zone (left part of the camera images in Fig. 3). The reflection of the dots and then their images on the two cameras is different in the wet and dry zones (the wet zone being fuzzy and brighter) making their detection in the wet zone difficult. However, it will be seen in the following that the method used for the detection in the present study allows the detection of nearly all the projected dots. The method is based on the pattern recognition technique developed by Ferré and Giralt (1989). The detection technique can be summarised as follows for each camera referred by superscript $j$.

First, a mask is systematically applied to each recorded image to extract the zone of interest (illuminated zone with dots). In particular, the useless parts of the images including the side wall of the flume (visible in Fig. 3(a) and (b)) are removed by applying this mask.

Then, a binary dot pattern of radius similar to the radius of the images of the dots (~12 pixels) of the illuminated zone is defined (see

Fig. 4(a)). This binary pattern is used as a template to compute the first correlation map $C_1^j$ with the image recorded by camera $j$ (Fig. 3) where the subscript refers to the first correlation. The local maxima $C_{1,k}^j$ of $C_1^j$ correspond to a first estimation of the position of the image-dot centres on each camera with dot index $k$, where $k=1:n_k$ and $n_k \leq 1470$ is the number of detected points. In order to maximise the number of dots that can be detected but also increase the accuracy of the detection of the image-dot centres, a second correlation map $C_2^j$ is computed using a new estimation of the dot pattern as a new template. The new template (see Fig. 4(b)) is an averaged pattern of the detected dots obtained from the first correlation $C_1^j$. For that, only the detected image-dots for which the local maxima $C_{1,k}^j$ satisfy $C_{1,k}^j > 3 \times \mathrm{RMS}(C_1^j)$ are considered. This criterion selects image-dots which correspond to the cleanest reflections of the patterns on the dry surface. Local maxima $C_{2,k}^j$ of the second correlation map $C_2^j$ with this new image-based template yield improved positions of the centres of the image-dots. The accuracy of this detection process is again improved using a subpixel Gaussian interpolation (Willert and Gharib, 1991). The sub-pixel position of $P_k^j$ on each camera image is referred hereafter as $P_{k|d.i.}^j = (u_k^j, v_k^j)$, $u_k^j$ and $v_k^j$ being expressed in sub-pixels and where *d.i.* stands for discrete image.

An example of the results obtained with this detection algorithm is shown in Fig. 5(a) and (b). The black crosses correspond to the coordinates $P_{k|d.i.}^1$ (a) and $P_{k|d.i.}^2$ (b) obtained from the detection algorithm. In this example, the number of detected point is $n_k = 1468$ on camera 1 and $n_k = 1461$ on camera 2, i.e. very close to the maximum of 1470. The detection algorithm is thus shown to be robust

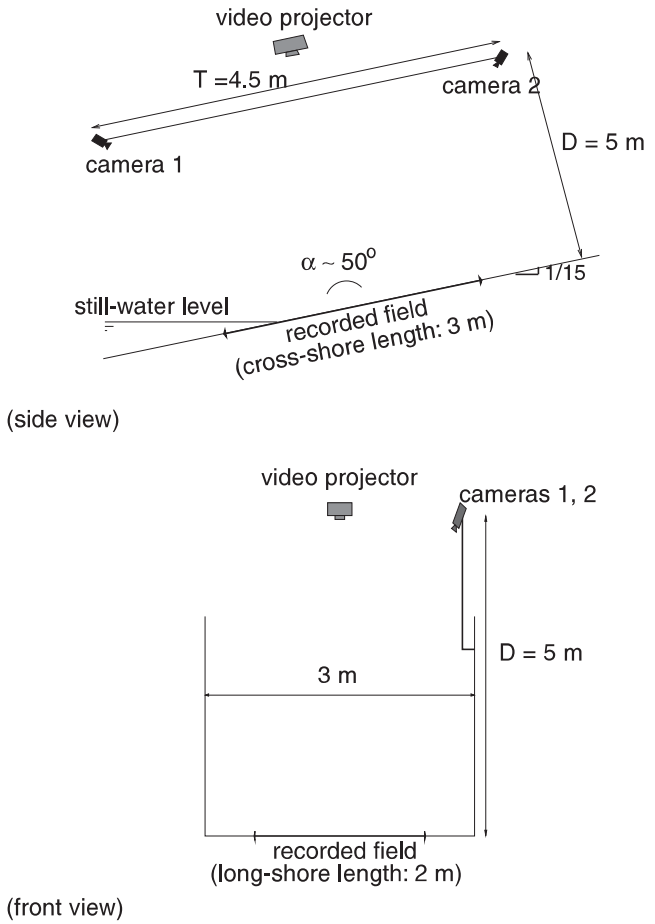


**Fig. 2.** Sketch of the stereovision system set-up (not to scale). The two cameras record the sand-bed in the swash zone (a $3 \times 2$ m$^2$ field). Dashed lines correspond to the optical axes of the cameras.

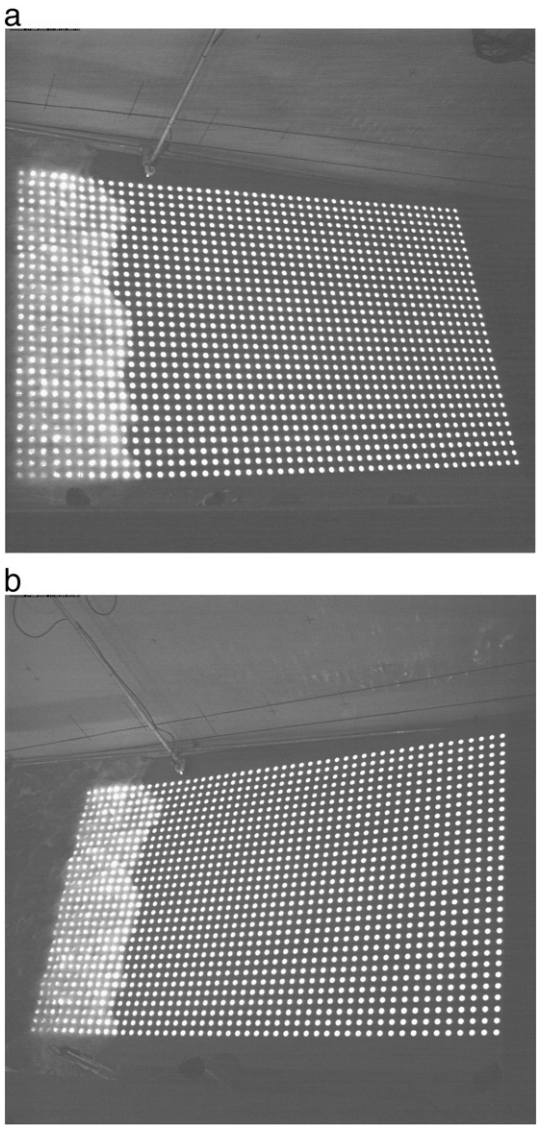


**Fig. 3.** Dot pattern projected on the swash zone with a video projector and imaged by camera 1 (a) and camera 2 (b).

and allows the determination of more than 98% of the dots in the dry zone and more than 90% of the dots in the wet zone.

The matching between the detected image-points $P_{k|d.i.}^1$ and $P_{k|d.i.}^2$ on camera 1 and camera 2, respectively, can be easily addressed thanks to the projected regular grid chosen. Image-points $P_{k|d.i.}^1$ and $P_{k|d.i.}^2$ are simply listed in a matrix ordered as the dot grid.

Once the image-points are detected on each camera and matched between the two cameras, the 3D metric position in the world coordinates, $P_{k|w}$, of the corresponding point $P_k$ is determined using a triangulation method, which is the central part of the stereovision technique. The general principle of this technique is described in the following. It will be shown that such a technique requires a calibration in order to estimate the optical properties of the system of cameras.

### 2.3. Stereovision: general principle

As mentioned above, triangulation is the identification of the intersecting point between the two different lines of sight –rays– passing through the two image points $P_k^1$ and $P_k^2$ (see Fig. 1) of the point $P_k$ in the laboratory frame of reference (i.e. in the world coordinates). The position of $P_k$ will be noted $P_{k|w} = (x_w, y_w, z_w)$ in the world coordinate frame of reference. The characterisation of the lines of

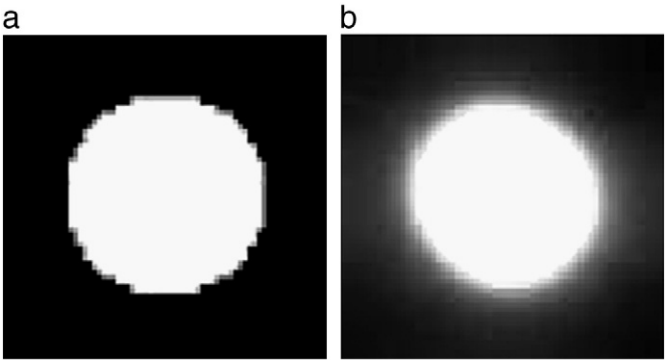


**Fig. 4.** (a) Initial template: a black and white binary pattern of the size of a typical projected dot. (b) Second template used for the second pass of correlation ($C^i_2$) and obtained by averaging all dots found above a certain threshold by the first correlation of an image($C^i_1$).

sight, and thus the triangulation process, requires the modelling of the camera's optical system (Salvi et al., 2005). In the present study the so-called pinhole camera model has been used, i.e., the image plane, is the camera sensor plane modelled by the pinhole camera model.

The pinhole camera model supposes that all the optical rays associated with a camera intersect at a single point, say $O^1$ for camera 1 and $O^2$ for camera 2 (see Figs. 1 and 6). The frame of reference centred at $O^j$ with axes $x^j_o$, $y^j_o$ aligned with the edges of the corresponding image plane and $z^j_o$ along the optical axis ($j$ being 1 or 2 depending on the considered camera) will be referred as the camera frame of reference (Fig. 6). The centre of each image plane, $O^j$, is then defined as the intersection of the optical axis $z^j_o$ with the image plane for each camera. In the discrete image frame associated to the image plane, point coordinates $(u,v)$ are in pixels and the origin is usually taken to be a corner of the image plane (see Fig. 6). In this last frame of reference, the coordinates of points $O^j$ and $P^j_k$ will be noted $O^j_{|d.i.} = (u^j_0, v^j_0)$ and $P^j_{k|d.i.} = (u^j_k, v^j_k)$, respectively (where *d.i.* stands for discrete image, as before). Following Calluaud and David (2004), it can be shown that $P^j_{k|d.i.}$ can be geometrically evaluated from $P_{k|w}$ with the transformation

$$s\left[P^j_{k|d.i.},1\right]^T = \mathbf{K}^j \cdot \mathbf{T}^j \cdot \left[P_{k|w},1\right]^T, \tag{1}$$

with $s$ an arbitrary scale factor (Sutton et al., 2009) and where

$$\mathbf{K}^j = \begin{pmatrix} k^j_u \cdot f^j & 0 & u^j_0 & 0 \\ 0 & k^j_u \cdot f^j & u^j_0 & 0 \\ 0 & 0 & 1 & 0 \end{pmatrix}, \quad \mathbf{T}^j = \begin{pmatrix} R^j & t^j \\ 0 & 1 \end{pmatrix}$$

for cameras $j=1$ and $j=2$.

The transformation (1) represents the projection from a 3D frame to a 2D frame and highlights the loss of one dimension by imaging with a single camera. $\mathbf{K}^j$ represents the internal transformation of the optical system and is defined by the intrinsic parameters $f^j$ (focal length), $k^j_u$ and $k^j_v$ (scale factor couple) and $u^j_0$, $v^j_0$, whilst $\mathbf{T}^j$ represents the external transformation of the optical system defined by $\mathbf{R}^j$ (the rotation matrix) and $\mathbf{t}^j$ (the translation vector) which give the orientation and position, respectively, of the camera with respect to the laboratory frame of reference. All these parameters have to be determined for each camera. The procedure via calibration will be discussed in the following section. It can be noted that the focal length $f$ and the scale factor couple $(k_u, k_v)$ cannot be dissociated, meaning that the model would be equivalent for two different optical systems as long as $(k_u \cdot f, k_v \cdot f)$ remain the same.

If $\mathbf{K}^j$ and $\mathbf{T}^j$ are known for each camera ($j=1$ and $j=2$), it can be easily shown that an unknown point $P_k$ of coordinates $P_{k|w}$ in the laboratory frame can be reconstructed by the triangulation of the measured image points $P^1_{k|d.i.} = (u^1_k, v^1_k)$ and $P^2_{k|d.i.} = (u^2_k, v^2_k)$ on each camera (see Hartley and Zisserman, 2004). The triangulation between two image points thus allows one to recover the third missing dimension when the projective transformation from $P_{k|w}$ to $P^j_{k|d.i.}$ (Eq. (1)) on a given image plane is used. The triangulation is the resolution of a system of 4 equations (resulting from Eq. (1) for the two cameras) for 3 unknowns of $P_{k|w}$, i.e. $x_w, y_w, z_w$:

$$u^j_k = k^j_u f^j \frac{\mathbf{R}^j_1 P_{k|w} + \mathbf{t}^j_1}{\mathbf{R}^j_3 P_{k|w} + \mathbf{t}^j_3} + u^j_0 \quad j = 1,2 \tag{2}$$

$$v^j_k = k^j_u f^j \frac{\mathbf{R}^j_2 P_{k|w} + \mathbf{t}^j_2}{\mathbf{R}^j_3 P_{k|w} + \mathbf{t}^j_3} + v^j_0 \quad j = 1,2 \tag{3}$$

where the subscripts 1, 2 and 3 correspond to the first, second and third lines (resp. elements) of the associated rotation matrix (resp. translation vector).

As shown, the modelling of the optical camera system implies a given number of unknown intrinsic and extrinsic parameters for each camera which have to be determined using a calibration process to be described in the two following sections. In particular, a global stereo calibration, which calibrates the system as a whole, will be used here since it is more accurate (Garcia et al., 2000). As in Heikkilä and Silvén (1997), three radial and two tangential distortion parameters are introduced to take into account the distortion of the images induced by the optical system. These parameters can be easily added to the intrinsic parameters matrix $\mathbf{K}^j$, the general concept described below being unchanged.

### 2.4. Stereovision calibration

The calibration method developed in the present study follows the procedure described by Bouguet (2004). For the calibration technique, a given number of points $P$ with known world coordinates $P_{|w}$ are imaged by the two cameras. Then, the method to evaluate the different parameters is based on the minimisation of the distance between the detected image points $P^j_{|d.i.} = (u^j, v^j)$ of $P$ on each image plane $j$ and the transformation of the known $P_{|w}$ through relation (1).

For the calibration procedure, a flat plate ($50 \times 50$ cm$^2$) (the model plane) marked with regularly spaced white dots on a black background has been used (see Fig. 7). First, several images of the model plane are captured by the two cameras under different orientations and positions. Then, each dot centre is detected for both image pairs using a correlation method based on a mean dot image (similar to the one discussed in the previous section). For the calibration process, the origin as well as the axes of the world system is attached to the model plane, in particular the $x_{|w}$ and $y_{|w}$ axes are aligned with the edge of the model plane and the $z_{|w}$ axis is perpendicular. Therefore, the world coordinates of each dot of the model plane are fixed by the geometry of the flat plate with a given accurate distance between the dots ($\Delta x = \Delta y = 5$ cm $\pm 60$ μm). The knowledge of the positions of the model plane's dots in the world frame of reference thus allows one to recover the unknown intrinsic and extrinsic parameters involved in Eq. (1). To this end, the cost function to minimise in the calibration process is the Euclidean back projection error of each point projected into the image plane. The best solution, in a least square sense, is approached by a non-linear optimisation algorithm, here the gradient descent method.

The cost function used for the calibration of one camera can be written

$$\theta = \sum_{l=1}^{n}\sum_{i=1}^{p}\left|\left|\left[p^j|d.i.,1\right]^T - \mathbf{K}\cdot\mathbf{T}\cdot\left[P_{|w},1\right]^T\right|\right|^2, \quad (4)$$

whilst it takes the form

$$\theta = \sum_{l=1}^{n}\sum_{i=1}^{p}\left(\left|\left|\left[P^1_{|d.i.},1\right]^T - \mathbf{K}^1\cdot\mathbf{T}^1\cdot\left[P_{|w},1\right]^T\right|\right|^2 + \left|\left|\left[P^2_{|d.i.},1\right]^T - \mathbf{K}^2\cdot\mathbf{T}^s\mathbf{T}^1\cdot\left[P_{|w},1\right]^T\right|\right|^2\right) \quad (5)$$

for the global stereovision calibration where $p$ is the number of points on the dot target and $n$ is the number of orientations acquired for the calibration process. As suggested in Zhang (2000), $n=8$ was used here. As the model plane is small compared to the size of the field of interest, for obvious practical reasons, attention was paid to place the model plane at different locations of the recorded field (Fig. 7).

The global stereovision calibration used in the present study assumes that instead of formulating the transformations $\mathbf{T}^j$, $j=1,2$,

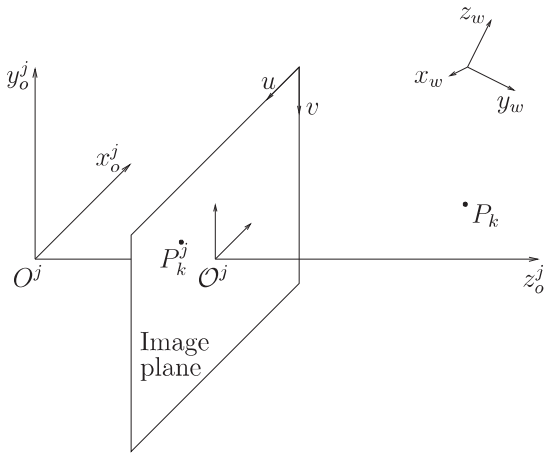


**Fig. 6.** Pinhole camera model: relation between a 3D point and its 2D image projection for camera $j$ ($j$ being 1 or 2).

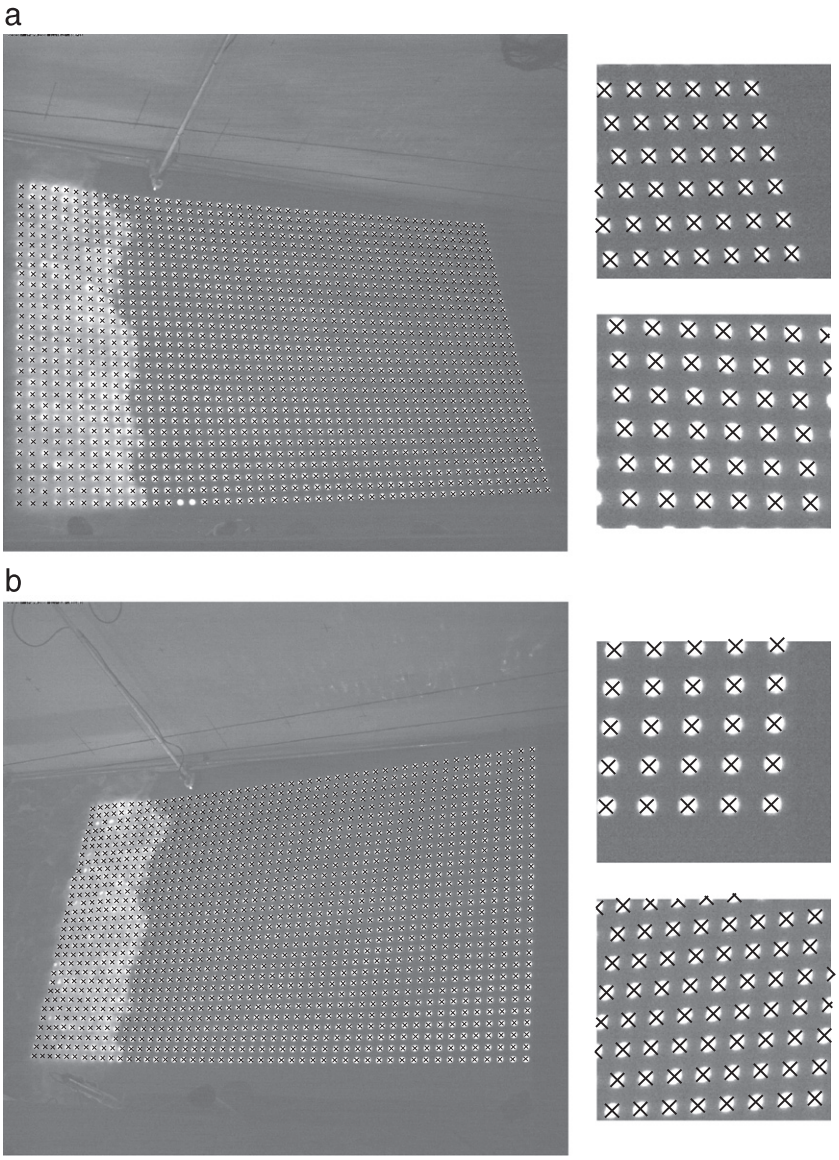


**Fig. 5.** Position of the image points $P_k^1$ and $P_k^2$ (crosses) detected on camera 1 (a) and camera 2 (b), respectively. Zooms at two different locations of the recorded field are also presented for both cameras.


**Fig. 7.** The 8 different views superposed on one image of the model plane for the global calibration of the stereovision system.

independently, they will be derived with respect to one of the two cameras, say camera 1. The transformations induced by rotation and translation $\mathbf{T}^2$ of camera 2 with respect to the world frame of reference is thus formulated using the transformation between the two camera frames, called $\mathbf{T}^s$, i.e. $\mathbf{T}^2 = \mathbf{T}^s\mathbf{T}^1$. This method does not change the general principle of the technique but generally leads to a better estimation of the three-dimensional reconstruction (Garcia et al., 2000).

In order to improve upon the convergence of the cost function minimisation (Eq. (5)), in the present study both cameras were first independently calibrated using Eq. (4), and the results were then used as initial values for the global stereovision calibration (Eq. (5)). This initialisation method is widely used in the literature (Benetazzo, 2006), and has shown better accuracy of the calibrating parameters. In the calibration algorithm (Bouguet, 2004) used herein, the intrinsic parameters are initialised for the first calibration (Eq. (4)) of each camera, as follows: (i) the principal point coordinates $O^j|_{d.i.}$ are set at the centre of the image plane; (ii) the focal length $f$ is initialised by estimating the field of view angle and the resolution of the sensor; (iii) the distortion coefficients are set to zero.

Using this calibration method, only $\mathbf{T}^1$ is view dependent, all the other parameters converge to a single value whatever the position of the image plane is. This is the principal reasons for the better accuracy of the global stereo calibration. $\mathbf{T}^1$ can then be easily defined using a model plane with known orientation and position in the world frame. In our case, a horizontal model plane is used to define the horizontal plane $(x,y)$ with $x$ being aligned with the water flume, $y$ and $z$ being the transverse and vertical directions, respectively. To this end, the model plane was positioned thanks to an electronic digital level with an accuracy of $\pm 0.1^o$. The orientation of the vertical direction $z$ is therefore defined within this accuracy. The directions of $x$ and $y$ were set according to the orientation of the vertical walls.

As discussed in Lavest et al. (1998), the calibration procedure is mainly affected by the quality of feature extraction in the calibration pattern images. In a projective transformation, every straight line in space given by a row of dots is imaged as a straight line onto the camera sensor. The precision of the feature extraction can thus be quantified by the residual error of each fitted line reconstructed with undistorted target images. Typical RMS errors were found to be about 0.03 and 0.05 pixels in each direction of the image planes.

### 2.5. Estimation of the errors

The errors in the estimation of the position of a point, inherent to the stereo technique, are called the quantization, or resolution, error. As proposed by Benetazzo (2006), the maximum quantization error $(er_{\hat{\mathbf{Z}}}, er_{\hat{\mathbf{X}}}, er_{\hat{\mathbf{Y}}})$ can be estimated theoretically such as:

$$er_{\hat{\mathbf{Z}}} = \frac{D^2}{2T\,N}\frac{sin(2\beta)}{cos\,(\beta+\alpha)^2},$$

$$er_{\hat{\mathbf{X}}} = \frac{D^2}{2N}\frac{sin(2\beta)}{cos\,(\beta+\alpha)^2},$$

$$er_{\hat{\mathbf{Y}}} = \frac{D^2}{2N}\frac{sin(2\beta)}{cos\,(\beta)^2},$$

with the $\hat{\mathbf{X}}$ axis aligned with the baseline, the $\hat{\mathbf{Z}}$ axis perpendicular to the $\hat{\mathbf{X}}$ axis and pointing towards the measured field and the $\hat{\mathbf{Y}}$ axis the transverse direction. $D$ and $T$ are the distances from the baseline and between the two cameras, respectively, and $\alpha$ is the angle between the cameras' lines of sight (see Fig. 2). $N$ is the number of pixels in one direction of the sensor and $\beta$ corresponds to half the angle of view of the cameras. In the present case ($\alpha = 50^o$, $\beta = 17.5^o$, $T = 4.5$ m, $D = 5$ m and $N = 2048$), we obtain $er_{\hat{\mathbf{Z}}} \sim 1430\,\mu$m, $er_{\hat{\mathbf{Y}}} \sim 1290\,\mu$m and $er_{\hat{\mathbf{Y}}} \sim 770\,\mu$m.

Using a similar stereo process, de Vries et al. (2011) estimated the actual accuracy of their technique to be ten times smaller than the theoretical prediction of formulas (2.5), the reason of the improvement being partly attributed to a sub-pixel algorithm. As mentioned in Section 2.4, the sub-pixel algorithm used here gives an error on the estimation of the image dots positions of 0.03 pix and 0.05 pix in each direction of the image plane. One can then assume that, with the sub-pixel algorithm, $N$ could be replaced by 20 $N$ in formulas (2.5) to evaluate the maximum quantization error in the present case. The estimation of the maximum quantization error, and therefore the theoretical indicative accuracy of the stereo technique, is reduced to $er_{\hat{\mathbf{Z}}} \sim 72\,\mu$m, $er_{\hat{\mathbf{X}}} \sim 65\,\mu$m and $er_{\hat{\mathbf{Y}}} \sim 39\,\mu$m.

A method to evaluate the accuracy of the present stereo technique is the reconstruction of the known positions of the dots on the model plane. The reconstruction of a horizontal model plane (rows of dots being aligned with the $x$ and $y$ directions) and a vertical model plane (rows of dots being aligned with the $x$ and $z$ directions) at two different locations of the recorded field, leads to a mean value of the distance between dots of $\Delta x = 4.98$ cm, $\Delta y = 4.99$ cm and $\Delta z = 4.97$ cm. This correspond to a bias error of the distance between dots of 200 μm, 100 μm and 300 μm in the $x$, $y$ and $z$ directions respectively, including the error of the calibration plate. The obtained accuracy is thus comparable to the size of a sand grain. The precision, given by the RMS errors of the dot distances, is also less than 300 μm.

Beyond the accuracy of the stereo method, errors can be induced by undesired movements of the system supporting both the cameras and the video projector. In order to estimate this error on the time scale of the experiment, a fixed point (a mark on the wall) is monitored during 30 min (a typical time series, see Section 3.1). In particular, it was found that no bias was induced by possible movements. On the other hand, small vibrations of the system can affect the precision of the measurements. The RMS error on the estimated position of the fixed point, associated to these vibrations, gives a precision of less than 400 μm.

Finally, the precision of the measurements can also be affected by the uncertainty of the form of the projected light dots on a rough sand surface as well as light beam fluctuations. To evaluate this uncertainty, positions of all the projected dots on the dry beach are estimated for several successive images before starting the wave paddle, the beach being therefore unchanged in time. The RMS error of the

variation of the measured position of the dots between the successive images gives a precision below 600 μm.

To conclude, the accuracy of the stereo process is estimated to be less than 300 μm, whilst the precision of the measure is less than 600 μm.

## 3. Hydralab III/SANDS experiments

### 3.1. Experimental set-up

The stereovision technique described above has been deployed during the HYDRALAB III/SANDS experiment in the large (100 m long and 3 m wide) wave flume CIEM (see Fig. 8). The wave-paddle can generate any complex surface wave spectrum, such as the Jonswap spectrum. A 1/15 sloping beach in the nearshore zone consisting of a well-sorted medium sand ($d_{50}=250$ μm) was built. The entire experiment consists of 39 repeated time series, *TS*, of 30 min duration during which the same paddle signal corresponding to a Jonswap spectrum (peak enhancement factor $\gamma=3.3$) is imposed for the waves. The generated waves reproduce erosive conditions with a significant wave height $H_s=0.53$ m and a peak period $T_p=4.14$ s. The reader should refer to Alsina and Cáceres (2010)) for more information on the experimental set-up. The time $t_s$ associated with a time series *TS* is defined such that $t_s=0$ at the beginning of each time series. The absolute time of reference $t=0$ corresponds to $t_s=0$ of the first time series ($TS=1$). In the present paper, each time series is sampled at 5 Hz for five selected intervals of 1 min duration that will be referred to as bursts hereafter.

The frame of reference (Fig. 8) is chosen such that $x$ is aligned with the principal direction of the wave flume (cross-shore direction), $z$ in the negative gravity direction and $y$ in the transverse direction (long-shore direction). The origin of this frame is such that $x=0$ at the rest paddle position, $y=0$ at the back side wall of the wave flume and $z=0$ at 3.13 m above the bottom of the flume. At the beginning of the experiment, the still-water level corresponds to $z=-66$ cm. The origin of $z$ was chosen for convenience using a mark on the back side wall of the flume.

### 3.2. Dry vs. wet surface distinction

An example of the 3D reconstruction given by the stereovision technique of the surface level $z=h(x,y,t)$ is shown in Fig. 9 at a given time ($t_s=897$ s within burst 3 of $TS=10$). This map corresponds to the raw images shown in Fig. 5. As observed in Fig. 9, the stereovision technique allows the surface $h(x,y,t)$ to be quantified in the dry area but also gives at least qualitative information in the wet area. It is thus possible to identify the water front at each time step and a criterion

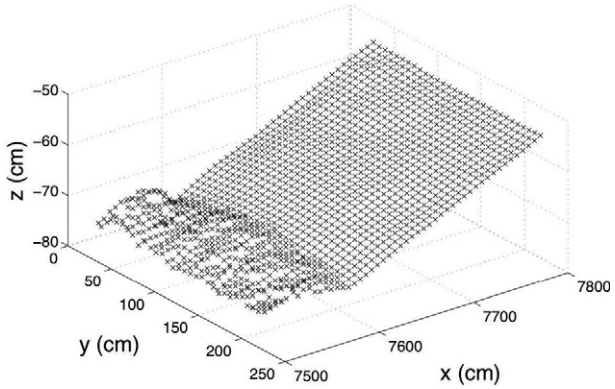


**Fig. 9.** An example of the 3D reconstruction of the surface level $z=h(x,y,t)$ in the swash zone at $t_s=897$ s (burst 3 of $TS=10$).

characterising the state (wet or dry) of the measured surface $h(x,y,t)$ can be proposed. This criterion is based on the fact that, as observed by Turner et al. (2008), the surface $h(x,y,t)$ rapidly varies in time as the water front passes through (see Fig. 10) whilst $h(x,y,t)$ remains essentially independent of time between swash events (dry beach). In Fig. 10 is shown $h$ and its temporal derivative $\partial h/\partial t$ as a function of time (within burst 5 of $TS=10$) at a given position ($x=7700$ cm and $y=150$ cm) where changes in dry and wet surfaces appear to occur. Intervals of almost constant $h$ are observed in Fig. 10. $\partial h/\partial t$ appears to be a good candidate to distinguish dry and wet areas in the swash zone.

Fig. 11 shows the evolution of $|\partial <h>_y/\partial t|$ in the $(t_s, TS\leq 25)$ plane at $x=7700$ cm for burst 5 ($1650\text{ s}\leq t_s\leq 1710$ s) where $<h>_y(x,t)$ corresponds to the average value of $h(x,y,t)$ along the transverse direction $y$. Given that the wave front varies much more significantly in the cross-shore direction $x$ than the long-shore direction $y$, considering $<h>_y(x,t)$ allows one to more clearly identify the cross-shore swash dynamics than a single profile for $y=$constant. In Fig. 11, black regions, i.e. low $\partial <h>_y/\partial t$, correspond to dry periods whilst white zones highlight the presence of water at the considered position. (The horizontal black line observed at $TS=6$ is due to a lack of information for this time series.) Three dry periods which are nearly independent of the time series *TS* are observed within this burst. As the same forcing is imposed in the different time series, this Figure thus shows a very strong correlation between the wave forcing and the swash zone hydrodynamics. A period of around 25 s can be deduced from the observation of these three dry periods, corresponding to the incident long-waves (Alsina and Cáceres, 2010). These standing long-waves are the signature of a random wave forcing on a dissipative beach (Masselink and Puleo, 2006) in accordance with the

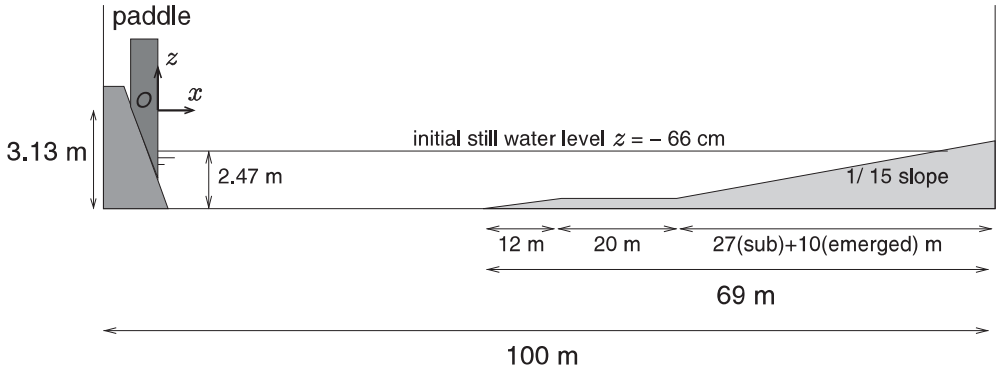


**Fig. 8.** Sketch of the UPC wave flume: the initial nearshore sand-bed profile is a 1/15 slope.

Iribarren parameter of 0.4 characterising the present experiment (Alsina and Cáceres, 2010). It should be noted that a fourth smaller dry period is observed around $t_s \sim 1690$ s. However, this dry period tends to disappear around $TS = 10$. This behaviour highlights a modification of the sand-bed shape during the experiment which is probably due to the global erosion of the beach in the nearshore zone as well as the signature of higher frequency incident waves.

For a quantitative description of the bed evolution, it has been arbitrarily chosen to define the dry region as $|\partial h/\partial t| < 0.05$ cm/s, as chosen by Turner et al. (2008). This threshold allows one to highlight the pertinence of the present technique to extract accurate quantitative information in the swash zone as shown in the following.

### 3.3. Sand-bed evolution

Using the threshold just defined, cross-shore profiles $z = <h>_y(x,t)$ of the sand level were extracted at different times (solid lines in Fig. 12). It can be seen that the wave forcing induces a global erosion in the nearshore zone, as expected from the Jonswap spectrum characteristics (Alsina and Cáceres, 2010). As observed from the solid lines in Fig. (12), the bed level does not reach a stationary shape for the times considered here. In Fig. 12, the obtained bed profiles $z = <h>_y(x,t)$ are also compared with data obtained from a standard mechanical bottom profiler at the centre of the flume $y = 150$ cm (Cáceres et al., 2008), performed every 3 or 4 *TS*. The resulting profiles (dashed lines in Fig. 12) show a good quantitative agreement, the difference being less than one centimetre which is roughly the margin of error of the bed profiler, but can also be attributed to long-shore variations as deduced from the stereovision technique and not accounted for with the mechanical profiler.

The stereovision technique developed in the present study allows one to have access to all relevant temporal scales of the spatial evolution of the bed level. The time-series scale evolution can be seen in Fig. 13(a) and (b) which reveal the evolving long-time erosive process at three spatial locations. Here the absolute time $t$ starting at the first *TS* is non-dimensionalised by the peak period $T_p = 4.14$ s and it can be seen that the measurements span over 10 000 $T_p$ (the first 23 *TS* where $1TS \sim 430T_p$). The three chosen spatial locations (of the 1600 measured) are $A_1 = (x,y) = (7750\text{ cm},\ 150\text{ cm})$, $A_2 = (7750\text{ cm}, 60\text{ cm})$ and $A_3 = (7650\text{ cm}, 150\text{ cm})$ in the swash zone, $A_1$ and $A_3$ being on the same cross-shore profile at the middle of the flume and $A_1$ and $A_2$ on the same long-shore profile. Fig. 13(a) shows the absolute bed level $z = h(x_n, y_n, t)$ whilst Fig. 13(b) shows

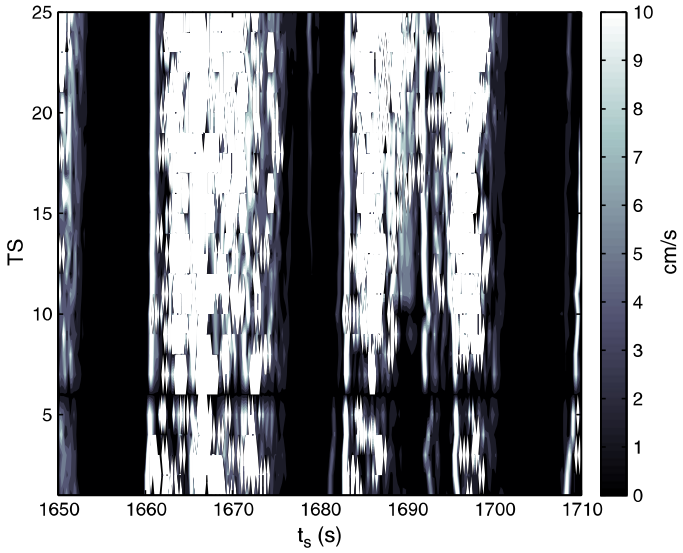


**Fig. 11.** $(t_s, TS \leq 25)$ diagram of $|\partial <h>_y/\partial t|$ at $x = 7700$ cm (burst 5). The horizontal axis represents the temporal evolution within burst 5 whilst the vertical axis corresponds to the different time series *TS*. (For each horizontal line, the same forcing is imposed by the wave paddle.)

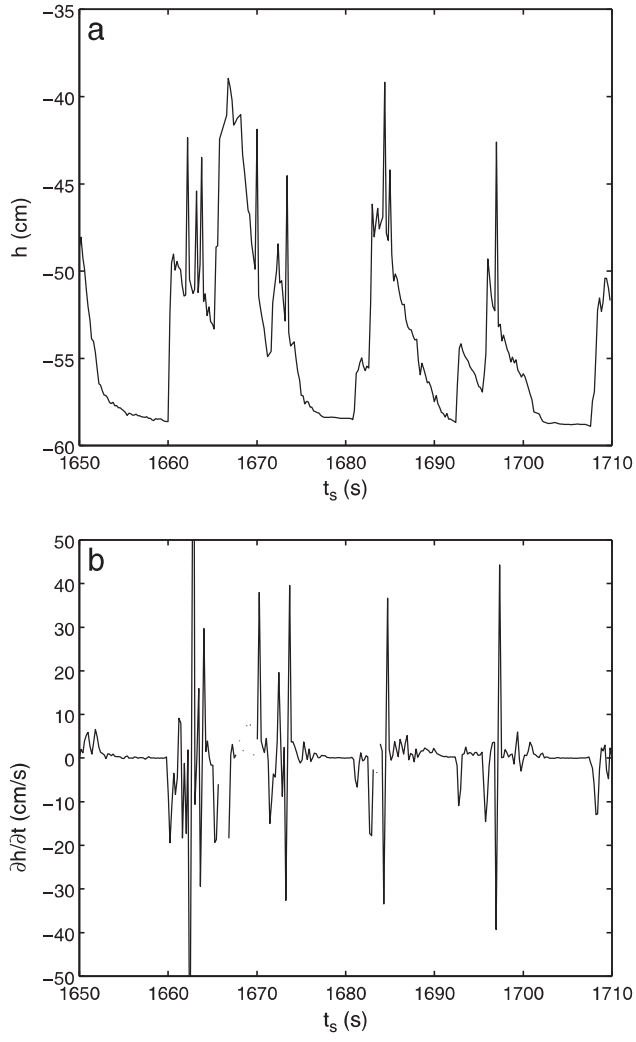


**Fig. 10.** Temporal evolution during burst 5 of $TS = 10$ of the measured surface elevation $h$ at $x = 7700$ cm and $y = 150$ cm (a), and its temporal derivative (b).

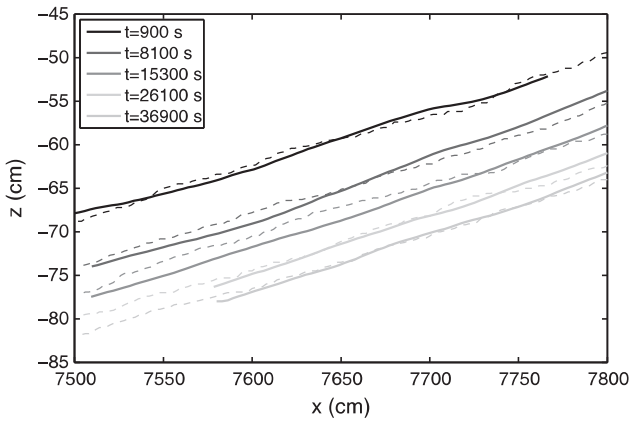


**Fig. 12.** Cross-shore profiles $z = <h>_y(x,t)$ of the bed level at different times obtained from the stereovision technique (solid lines). Cross-shore profile $z = h(x,t)$ extracted from mechanical profiler data at $y = 150$ cm at the centre of the flume (dashed lines).

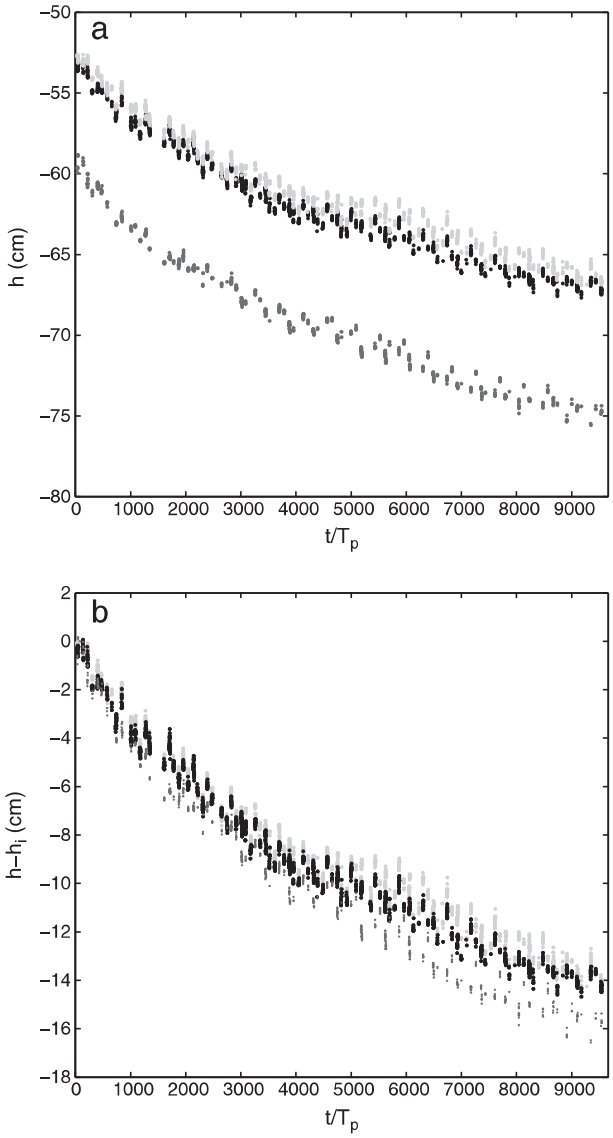


**Fig. 13.** Temporal evolution of the sand-bed surface $h(x,y,t)$ (a) at three different locations in the swash zone, $A_1$ (black dots), $A_2$ (light grey dots) and $A_3$ (dark grey dots) (see text for details). Time is non-dimensionalised by the peak period $T_p$ of the Jonswap forcing. The erosive process is highlighted by subtracting the initial bed level $h_i(x,y)=h(x,y,t=0)$ at the three positions respectively (b).

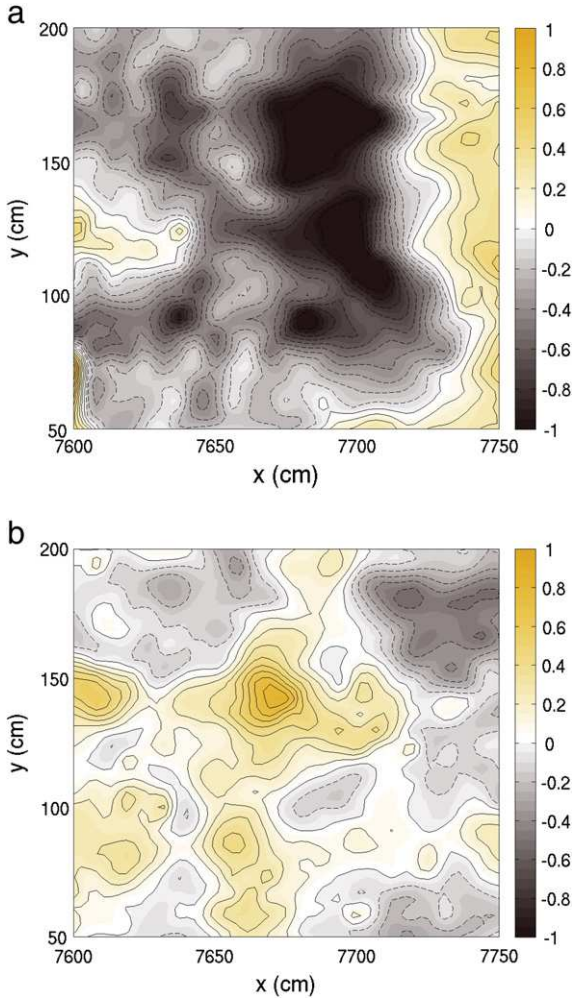


**Fig. 14.** Contour field of the sand-bed variation $\Delta h$ between times $t_1$ and $t_2$: (a) $t_2-t_1=27$ s $\sim 6T_p$ (in burst 1, $TS=1$, $t_{s/1}=7.2$ s), (b) $t_2-t_1=47$ s $\sim 12T_p$ (in burst 5, $TS=1$, $t_{s/1}=9$ s).

the relative change in bed height $h(x_n,y_n,t)-h_i(x_n,y_n)$ where $h_i(x_n,y_n)=h_i(x_n,y_n,t=0)$ and $n$ are positions 1,2,3. In both Figures, a global decrease or erosion can be observed. The $h$ or $h-h_i$ variations on much shorten time-scales (wave scale) appear here as if they were vertical experimental scatter but in fact these variations are larger than the experimental error (<300 μm) and represent erosive and deposition acretive changes of 0.5 to 1 cm in bed height. The relative height evolution at the time-series scale in Fig. 13(b) allows one to discern that the global (in a temporal sense) erosion is spatially dependent. Indeed, it can be seen in Fig. 13(b) that whilst still decreasing (eroding), all three $h-h_i$ data sets diverge for $t/T_p>4000$, implying that the global erosion process is spatially inhomogeneous. More specifically, the relative erosion $h-h_i$ is larger for different cross-shore positions (between $A_1$ and $A_3$) but is also observed to vary in the long-shore direction (between $A_1$ and $A_2$).

The spatially dependent behaviour can also be examined in detail for the wave time-scales. This is done in Fig. 14(a) and (b) in which the relative bed evolution $\Delta h=h_2(x,y,t_2)-h_1(x,y,t_1)$ between times $t_1$ and $t_2$ is plotted for $t_2-t_1=27$ s $\sim 6T_p$ (in burst 1, $TS=1$, $t_{s/1}=7.2$ s) and $t_2-t_1=47$ s $\sim 12T_p$ (in burst 5, $TS=1$, $t_{s/1}=9$ s), respectively. Physically, $t_2-t_1$ in Fig. 14(a) corresponds to the interval of instantaneous wave forcing of a single incident standing long-wave period (~20 s) as observed by Alsina and Cáceres (2010) and $t_2-t_1$ in Fig. 14(b) to two such incident standing long-wave periods. It should also be noted that the type of forcing is different between both time intervals due to the irregular forcing. It can be seen in both Figures that regions of accretion coexist with regions of erosion, both of the order of 1 cm, i.e. undetectable with most current techniques, on the relative short time-scale of the incident long-wave. Comparison between Fig. 14(a) and (b) further show that this trend of spatially dependent regions of accretion and erosion strongly depends on the instantaneous wave forcing.

## 4. Conclusion

A stereoscopic technique is presented that allows the identification of the dry sand-bed areas in the swash zone as well as the bed elevation determination with high precision. This technique is temporally resolved at all relevant scales (from within a wave to the long-term beach evolution) over a large area of the swash zone (~2 m×3 m) with an accuracy below 300 μm, a precision of less than 600 μm and a spatial resolution of 5 cm. In particular, a variation

of the measured sand beach of less than 1 mm can therefore be considered as the true beach variation.

The experiments were performed in the large CIEM wave flume of the University of Catalunya during which a Jonswap spectrum forcing under erosive conditions was imposed. On the long time-scale, the presented technique reveals good agreement with the results of a classical mechanical profiler of the cross-shore profiles evolution and the associated erosion.

On the smaller time-scale (from wave by wave to several incident standing long-wave periods), it is shown that the variability is more complex than a continuous erosion, the picture arising from classical profiling measurements. In addition, spatially dependent zones of accretion or erosion are observed at small time-scales. Both highlight the complex hydrodynamics involved in the swash zone.

Application of this technique is expected to yield the necessary information to better understand and model the complex processes occurring in the swash zone.

## Acknowledgement

The data presented were obtained within the framework of the European Hydralab-III SANDS Project (contract number: 022441) (RII3).

## References

Aagaard, T., Hughes, M., 2010. Breaker turbulence and sediment suspension in the surf zone. Marine Geology 271, 250–259.
Alsina, J., Cáceres, I., 2010. Sediment suspension events in the inner surf and swash zone. Measurements in large-scale and high-energy wave conditions. Coastal Engineering 58, 657–670.
Baldock, T.E., Barnes, M.P., Hughes, M.G., 2006. Field observations of instantaneous cross-shore free surface profiles and flow depth in the swash zone. In: Sanchez-Archilla, A. (Ed.), Coastal Dynamics 2005 [CD-ROM]. ASCE, Reston, VA.
Benetazzo, A., 2006. Measurements of short water waves using stereo matched image sequences. Coastal Engineering 53, 1013–1032.
Bouguet, J.Y., 2004. Camera calibration toolbox for matlab. http://www.vision.caltech.edu/bouguetj/calib_doc/2004.
Butt, T., Russell, P., 2000. Hydrodynamics and cross-shore sediment transport in the swash-zone of natural beaches: a review. Journal of Coastal Research 16, 255–268.
Cáceres, I., Grüne, J., Rijn, L.V., Sánchez-Arcilla, A., Ahmari, A., Ribberink, J., 2008. Mobile bed tests, the sands project. 31st Int. Conf. Coastal Eng. ASCE.
Calluaud, D., David, L., 2004. Stereoscopic particle image velocimetry measurements of the flow around a surface-mounted block. Experiments in Fluids 36, 53–61.
Chatellier, L., Jarny, S., Gibouin, F., David, L., 2010. Stereoscopic measurement of free surface flows. 14th International Conference on Experimental Mechanics. Poitiers, France.
de Vries, S., Hill, D.F., de Schipper, M.A., Stive, M.J.F., 2011. Remote sensing of surf zone waves using stereo imaging. Coastal Engineering 58, 239–250.
Douxchamps, D., Devriendt, D., Capart, H., Craeye, C., Macq, B., Zech, Y., 2005. Stereoscopic and velocimetric reconstructions of the free surface topography of antidune flows. Experiments in Fluids 39, 533–551.
Elfrink, B., Baldock, T., 2002. Hydrodynamics and sediment transport in the swash zone: a review and perspectives. Coastal Engineering 45, 149–167.
Ferré, J.A., Giralt, F., 1989. Pattern-recognition analysis of the velocity field in plane turbulent wakes. Journal of Fluid Mechanics 198, 27–64.
Garcia, D., Orteu, J., Devy, M., 2000. Accurate calibration of a stereovision sensor: comparison of different approaches. Proceeding of 5th Fall Workshop on Vision, Modeling and Visualization. Saarbrücken, Germany.
Hartley, R., Zisserman, A., 2004. Multiple View Geometry in Computer Vision. Cambridge University Press.
Heikkilä, J., Silvén, O., 1997. A four-step camera calibration procedure with implicit image correction. IEEE Computer Society Conference on Computer Vision and Pattern Recognition, San Juan, Puerto Rico.
Holland, K., Holman, R., 1997. Video estimation of foreshore topography using trinocular stereo. Journal of Coastal Research 13, 81–87.
Holland, K., Puleo, J., 2001. Variable swash motions associated with foreshore profile change. Journal of Geophysical Research 196, 4613–4623.
Jehle, M., Jarny, S., David, L., 2008. Différentes approches pour la mesure d'interfaces et de surface libre. 11ème Congrès Francophone de Techniques Lasers, Poitiers, France, pp. 225–232. In French.
Lavest, J., Viala, M., Dhome, M., 1998. Do we really need an accurate calibration pattern to achieve a reliable camera calibration? Proc. ECCV98, Freiburg, Germany, pp. 158–174.
Lippmann, T., Holman, R., 1990. The spatial and temporal variability of sand bar morphology. Journal of Geophysical Research 95, 11,575–11,590.
Longo, S., Petti, M., Losada, I., 2002. Turbulence in the swash and surf zones: a review. Coastal Engineering 45, 129–147.
Masselink, G., Puleo, J., 2006. Swash-zone morphodynamics. Continental Shelf Research 26, 661–680.
Masselink, G., Evans, D., Hughes, M., Russel, P., 2005. Suspended sediment transport in the swash zone of a dissipative beach. Marine Geology 216, 169–189.
Salvi, J., Armangue, X., Battle, J., 2005. A comparative review of camera calibrating methods with accurcy evaluation. Pattern Recognition 35, 1617–1635.
Sutton, M.A., Orteu, J.J., Schreier, H., 2009. Image Correlation for Shape, Motion and Deformation Measurements Basic Concepts, Theory and Applications. Springer.
Turner, I., Russell, P., Butt, T., 2008. Measurement of wave-by-wave bed-levels in the swash zone. Coastal Engineering 55, 1237–1242.
Willert, C., Gharib, M., 1991. Digital particle image velocimetry. Experiments in Fluids 10, 181–193.
Zhang, Z., 2000. A flexible new technique for camera calibration. IEEE Transactions on Pattern Analysis and Machine Intelligence 22, 1330–1334.